ACS OMEGA

Article

Cite This: ACS Omega 2019, 4, 6375−6381

http://pubs.acs.org/journal/acsodf

Resolving the Ultrafast Changes of Chemically Inequivalent Metal−Ligand Bonds in Photoexcited Molecular Complexes with Transient X-ray Absorption Spectroscopy

Jianxin Zhang,[†] Xiaoyi Zhang,[‡] Karina Suarez-Alcantara,[§] Guy Jennings,[‡] Charles A. Kurtz,[‡] Latévi Max Lawson Daku,[∥] and Sophie E. Canton*[,⊥,#]

[†]State Key Laboratory of Hollow Fiber Membrane Materials and Processes, School of Environmental and Chemical Engineering, Tianjin Polytechnic University, Tianjin 300387, China

[‡]X-ray Science Division, Argonne National Laboratory, 9700 S. Cass Avenue, Lemont, Illinois 60439, United States

[§]UNAM-IIM Morelia, Antigua carretera a Pátzcuaro 8710, Col. Ex-hacienda de San José de la Huerta, Morelia, Michoacán 58190, México

[∥]Département de Chimie Physique, Université de Genève, Quai E. Ansermet 30, CH-1211 Genève 4, Switzerland

[⊥]ELI-ALPS, ELI-HU Non-Profit Ltd., Dugonics ter 13, Szeged 6720, Hungary

[#]Attosecond Science Group, Deutsches Elektronen Synchrotron (DESY), Notkestrasse 85, D-22607 Hamburg, Germany

Supporting Information

ABSTRACT: Photoactive transition-metal complexes that incorporate heteroleptic ligands present a first coordination shell, which is asymmetric. Although it is generally expected that the metal−ligand bond lengths respond differently to photoexcitation, resolving these fine structural changes remains experimentally challenging, especially for flexible multidentate ligands. In this work, ultrafast X-ray absorption spectroscopy is employed to capture directly the asymmetric elongations of chemically inequivalent metal−ligand bonds in the photoexcited spin-switching Fe^{II} complex $[Fe^{II}(tpen)]^{2+}$ solvated in acetonitrile, where tpen denotes *N*,*N*,*N*′,*N*′-tetrakis(2-pyridylmethyl)-1,2-ethylenediamine. The possibility to correlate precisely the nature of the donor/acceptor coordinating atoms to specific photoinduced structural changes within a binding motif will provide advanced diagnostics for optimizing numerous photoactive chemical and biological building blocks.

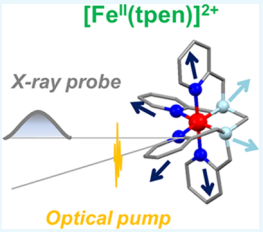

INTRODUCTION

Building efficient photoactive molecular complexes around transition-metal (TM) ions generally necessitates employing cagelike or heteroleptic ligands to promote the emergence of multifunctionality.[1−3] Such compounds frequently present an asymmetric first coordination sphere (1-CS) with chemically inequivalent metal−ligand (M−L) bond lengths.[4−7] The sensitive balance between electronic and geometric factors determines the ground-state properties and the reactivity patterns of the TM complexes. Geometric trends within series of closely related families manifest through similarities in M−L bond lengths and bond angles, which are revealed by systematic structural studies in solution and in the crystalline phase.[8−10] Such trends allow correlating the chemical composition and the connectivity of the ligands with the oxidation state and the coordination geometry of the metal ion. Electronic trends associated to the chemical functionalities (e.g., presence of aliphatic or aromatic groups) and to the donor/acceptor abilities of various ligands can be identified through nephelauxetic effects or spectroelectrochemical series. Such trends enable a detailed description of the synergetic covalency imparted by nonequivalent M−L bonds, which can be further influenced by solvation.[11−13] Once tested and validated, the comprehensive relationships between electronic and geometric structures can be employed as design principles to guide the synthetic strategies and to benchmark the descriptive−predictive power of the theoretical methods.

Gaining similar insights for photoexcited TM complexes is a crucial step toward devising novel covalent assemblies with excited-state manifolds that are tailored toward specific light-driven functionalities and operando robustness. However, due to inherently short lifetimes, the key metastable species are difficult to detect and their molecular geometries often stand insufficiently characterized. In particular, the response of the nonequivalent M−L bonds to photoexcitation can rarely be inferred from indirect measurements so that it tends to be postulated or calculated in most cases.

Owing to their intrinsic spatial and temporal resolutions, the ultrafast X-ray methods currently developed at synchrotron and X-ray free electron laser facilities can deliver atomistic diagnostics about energy-rich systems as they evolve rapidly after photoabsorption[14−17] Specifically, transient X-ray absorption spectroscopy (TXAS) has been successfully employed to quantify the alterations within the 1-CS of photoexcited spin-

Received: December 31, 2018
Accepted: March 27, 2019
Published: April 5, 2019

switching complexes in terms of average M−L bond length changes.[18−23] So far, very few studies have reported detecting unequal M−L bond elongations with satisfactory accuracy from the analysis of the near-edge region[24,25] and the extended range[26−28] of their TXAS spectra. The present work demonstrates how TXAS achieving a high signal-to-noise (S/N) ratio can resolve the ultrafast changes of chemically inequivalent M−L bonds in the photoexcited state of the prototypical spin-switching complex $[Fe^{II}(tpen)]^{2+}$ (where tpen denotes *N,N,N′,N′*-tetrakis(2-pyridylmethyl)-1,2-ethylenediamine) solvated in acetonitrile (CH_3CN).[29]

RESULTS AND DISCUSSION

The hexadentate tpen ligand is shown in Figure 1a. The 1-CS of the molecular complex $[Fe^{II}(tpen)]^{2+}$ (Figure 1b) comprises

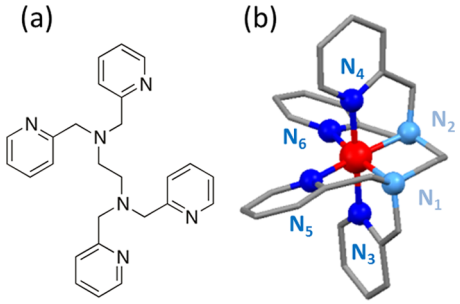

Figure 1. (a) Chemical structure of the free tpen ligand. (b) Molecular complex $[Fe^{II}(tpen)]^{2+}$. The two aliphatic nitrogen atoms are in cyan, whereas the four aromatic ones are in blue.

two inequivalent types of nitrogen (N) atoms, namely, two aliphatic N_1, N_2 (cyan) in the ethylendiamine linkage of the fused five-membered chelate rings coordinated in a cis fashion and four aromatic N_3, N_4, N_5, N_6 (blue) in the six-membered pyridine (cyclic imine) rings.

Depending on the crystallization conditions (e.g., solvents, counterions), $[Fe^{II}(tpen)]^{2+}$ exhibits different polymorphs.[29−32] Nevertheless, for all reported structures, the asymmetric coordination of the Fe^{II} ion induces a significant distortion in the 1-CS away from the octahedral (O_h) symmetry toward the quasi-D_{3h} symmetry through a trigonal twist of the two planes (N_1, N_3, N_5) and (N_2, N_4, N_6), whereas the pyridine planes remain nearly perpendicular to each other. The four Fe−$N_{aromatic}$ and the two Fe−$N_{aliphatic}$ are quasi-identical so that two inequivalent Fe−N bond lengths have to be considered for describing accurately the ground-state structure of $[Fe^{II}(tpen)]^{2+}$.

At room temperature, the complex in CH_3CN is in the ground state, where the Fe^{II} center is in the $(t_{2g})^6$ low-spin (LS) configuration.[29,33,34] Upon laser excitation at λ_{exc} = 400 nm, a fraction (f) of the molecules is promoted to the singlet Franck−Condon state that decays on the sub-picosecond time scale with a 100% yield into the metastable excited state where the Fe^{II} center is in the $(t_{2g})^4(e_g)^2$ high-spin (HS) configuration.[33−37] Figure 2a shows the $\mu_{laser\_on}(t)$ (blue trace) and μ_{laser_off} (black trace) normalized XAS spectra at the Fe K edge (E_0 = 7109 keV) for a pump−probe delay of t = 150 ps. The corresponding difference signal $\Delta\mu(\tau) = [\mu_{laser\_on}(t) - \mu_{laser\_off}]$ is displayed in Figure 2b.

Figure S1 displays the k^2-weighted EXAFS functions, $\chi(k)$, extracted from μ_{laser_off} (black) of $[Fe^{II}(tpen)]^{2+}$ solvated in CH_3CN and from μ_{powder} of the $[Fe^{II}(tpen)](PF_6)_2$ salt

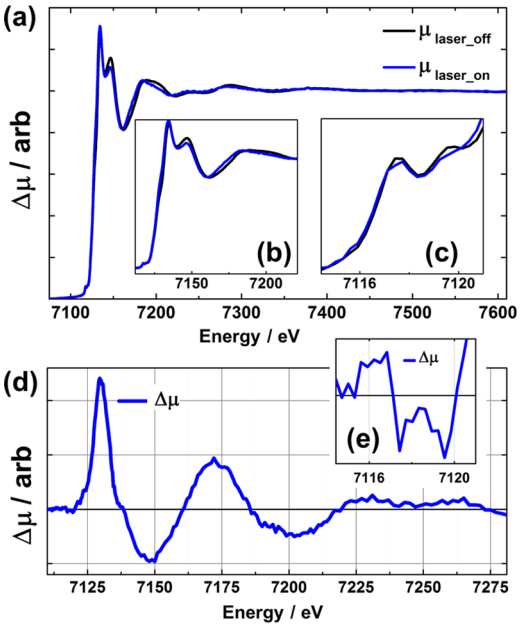

Figure 2. (a) $\mu_{laser\_on}(t)$ at 150 ps pump−probe delay (blue) and μ_{laser_off} (black) for $[Fe^{II}(tpen)]^{2+}$ in MeCN. The insets zoom on the near-edge region (b) and in the pre-edge region (c). (d) Corresponding transient difference X-ray spectrum $\Delta\mu(t) = [\mu_{laser\_on}(t) - \mu_{laser\_off}]$. The inset zooms on the pre-edge region (e).

(gray).[18] It should be noted that the traces are identical, ruling out any influence of solvation.

The lineshape of $\Delta\mu(t)$ in the near-edge region (inset Figure 2b) reflects the well-known spectral alterations due to the coupled changes in electronic and geometric structures triggered by the double population of the antibonding e_g orbital in the HS state of $[FeN_6]$ complexes.[21,26] The inset Figure 2c zooms on the pre-edge region. The splitting of the associated transition 1s → 3d, which is dipole-forbidden in the O_h symmetry, confirms the significant distortion of the 1-CS suggested by the crystal structures.

Considering the pronounced anisotropy of the Fe^{II} ion, it is clear that the analysis of the TXAS signal needs to go beyond quantifying the elongation of a single average Fe−N bond length. The established fitting methodology[19] is applied to extract the Fe−N_α and Fe−N_β of aromatic and aliphatic character from a fitting procedure where Fe−N_α and Fe−N_β constrained as ρ*Fe−N_α are chosen as free structural parameters for 1-CS. Since differences in distances between the metal ion and the nearest neighbors can manifest as a structural disorder, a single Debye−Waller factor was considered to allow distinguishing the contributions from two Fe−N bond lengths in the TXAS signal. Figure 3 shows the labeling of the atoms used in the analysis. Additional technical details are given in the Experimental Section.

Figure 4a,b contains the amplitude and the phase for the Fourier transform of $k^2\chi^*(k)$ in real (R) space for the LS and HS states, respectively, directly fitted from the μ_{laser_off} and $\mu_{laser\_on}(t)$ spectra. The parameters derived for the first- and second-coordination shells (1-CS and 2-CS) from the analysis are summarized in Table 1.

A value of 34 ± 7% is obtained for f (Figure 4c) from a least-square minimization procedure. Figure 4d shows the reconstructed $k^2*\chi(k)$ for the excited HS state spectrum. The Fe−$N_{aliphatic}$ and Fe−$N_{aromatic}$ differ by about 0.04 ± 0.04

DOI: 10.1021/acsomega.8b03688
ACS Omega 2019, 4, 6375−6381

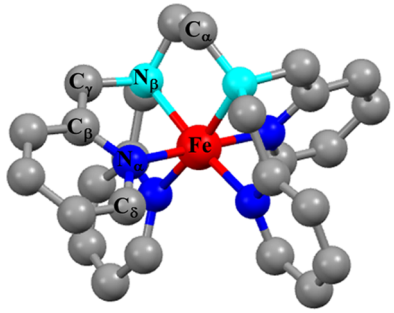

Figure 3. Labeling of the different N and C atoms included in the analysis of the TXAS signal.

Å in the LS state. This slight mismatch has been attributed to absence of π back-bonding from the saturated $N_{aliphatic}$ to the Fe^{II} center. The TXAS analysis that fits concurrently the LS and HS structures clearly captures two different bond elongations in the photoinduced HS state: $Fe-N_{aromatic}$ increases by 0.17 ± 0.04 Å, whereas $Fe-N_{aliphatic}$ increases by 0.24 ± 0.04 Å. In the HS state, the two bond lengths now differ by 0.11 ± 0.03 Å. The difference $\Delta R = (Fe-N_\beta) - (Fe-N_\alpha)$ and the ratio $\rho = Fe-N_\beta/Fe-N_\alpha$ for the structural parameters of the 1-CS are in excellent agreement with the results obtained from DFT optimization summarized for the LS and HS in Table 2.

It should be noted that a detailed comparison with crystallographic data cannot be provided due to the polymorphism exhibited by the complex. The increase in $Fe-N_{aromatic}$ (+0.17 Å) is shorter than the ∼+0.20 Å observed for $[Fe^{II}(bpy)_3]^{2+}$[12,13] and $[Fe^{II}(phen)_3]^{2+}$,[10] which both display 1-CS with six $N_{aromatic}$ nearest neighbors. The increase in $Fe-N_{aliphatic}$ (+0.24 Å) is comparable to the one displayed by the HS synthetic analogues.[38] This asymmetric bond elongation can be ascribed to an intricate σ-donation and π-back-donation

Table 1. Fit Parameters for the 1-CS and 2-CS of the LS and HS States for $[Fe^{II}(tpen)]^{2+}$ in CH_3CN[a]

	1-CS				
	ΔE (eV)	S_0^2	R_{Fe-N_α} (Å) (D = 4)	R_{Fe-N_β} (Å) (D = 2)	$\sigma_{Fe-N_{\alpha,\beta}}{}^2$
LS	−1.5	0.8	1.98	2.02	0.005
	±1.5	±0.2	±0.02	±0.02	±0.003
HS	0.4	*0.8*	2.15	2.26	*0.005*
	±1.3		±0.02	±0.02	

	2-CS					
	R_{Fe-C_α} (Å) (D = 4)	R_{Fe-C_β} (Å) (D = 4)	R_{Fe-C_γ} (Å) (D = 2)	$R_{Fe-C\delta}$ (Å) (D = 4)	$\sigma_{Fe-C_{\alpha,\beta,\gamma}}{}^2$	$\sigma_{Fe-N_{\alpha\beta}-C_{\alpha,\beta,\gamma,\delta}}{}^2$
LS	2.82	2.87	2.93	3.03	0.006	0.009
	±0.03	±0.03	±0.03	±0.03	±0.005	±0.011
HS	2.98	3.04	3.10	3.20	*0.006*	*0.009*
	±0.02	±0.02	±0.02	±0.02		

[a]The k range extended from 2 to 10 $Å^{-1}$. D indicates the degeneracy of the scattering paths in FEFF. The values kept constant during the optimization are indicated in italic. The corresponding excited state fraction (f) is 34 ± 7%.

Table 2. Comparison of the Aromatic and Aliphatic Fe−N Bond Distances in the LS and HS States of Solvated $[Fe(tpen)]^{2+}$ Obtained from the Experiment and the DFT Calculations

state	$Fe-N_{aromatic}$ ($Å^{-1}$)	$Fe-N_{aliphatic}$ ($Å^{-1}$)	difference Δ ($Å^{-1}$)	ratio ρ
LS (exp)	1.98 ± 0.02	2.02 ± 0.02	0.04 ± 0.03	1.02
HS (exp)	2.15 ± 0.02	2.26 ± 0.02	0.11 ± 0.03	1.05
ΔR_{exp}	0.17 ± 0.04	0.24 ± 0.04	0.07 ± 0.04	
LS	1.969	2.015	0.046	1.023
HS	2.163	2.275	0.112	1.052
ΔR_{theo}	0.194	0.260	0.066	

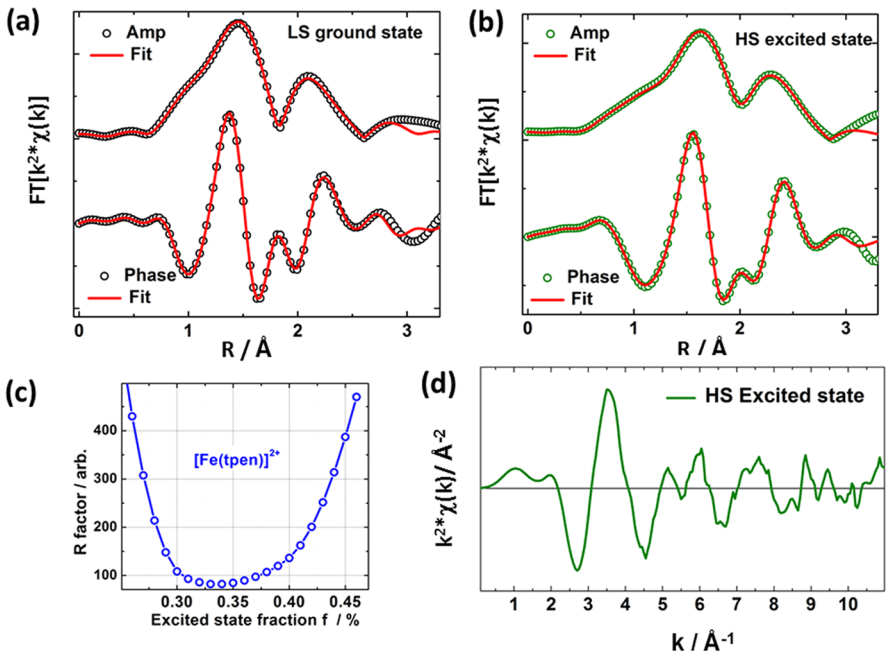

Figure 4. Amplitude and phase for the Fourier transform of the EXAFS function $k^2*\chi(k)$ along with the best fit for (a) LS ground state and (b) HS excited state. (c) Fitted excited state fraction (f); the best-fit value being 34 ± 7%. (d) EXAFS function, $k^2*\chi(k)$, of the HS excited state for $[Fe^{II}(tpen)]^{2+}$.

DOI: 10.1021/acsomega.8b03688
ACS Omega 2019, 4, 6375−6381

redistribution. Overall, the net structural effect of the photoinduced LS−HS transition is a large opening of the N_5−Fe−N_6 angle (where the two $N_{aromatic}$ atoms are located trans to $N_{aliphatic}$) from 109 to 132°, yielding an intraligand groove that should promote preferential interaction with solvent molecules. The detailed investigation of the solvation dynamics that accompanies the photoinduced spin-state transition in $[Fe^{II}(tpen)]^{2+}$ with combined picosecond and sub-picosecond transient X-ray spectroscopy and scattering will be presented in future reports.

CONCLUSIONS

In conclusion, the present study on the spin-switching complex $[Fe^{II}(tpen)]^{2+}$ solvated in CH_3CN illustrates the distinct strength of TXAS to extract reliable structural parameters for photoexcited complexes with multidentate ligand scaffolds that display polymorphism or that cannot be easily crystallized. Moreover, it can be expected that this structural technique will be generally employed to deliver advanced diagnostic about the ultrafast evolution of bond lengths in heteroleptic molecular complexes with definite sensitivity toward chemical functionalities.

EXPERIMENTAL SECTION

Materials. $[Fe^{II}(tpen)](PF_6)_2$ was synthesized according to the reported protocol.[29] All reagents were used as received from commercial sources without further purification.

DFT Optimizations. The DFT optimizations for the LS and HS states of $[Fe^{II}(tpen)]^{2+}$ solvated in CH_3CN were performed with the Gaussian09 program package [1] using the dispersion-corrected PBE-D3 functional [2] and the TZVP basis set of triple-zeta-polarized quality [3] and without symmetry constraints. Solvent effects were included with the polarizable continuum model using the integral equation formalism variant (IEFPCM) [4].

Transient X-ray Absorption Spectroscopy (TXAS). The transient X-ray absorption spectroscopy (TXAS) measurements were conducted at beamline 11-ID-D of the Advanced Photon Source (APS, Argonne National Laboratory). The configuration of the experimental optical pump X-ray probe setup was similar to the one used adequately in previous studies.[26,27] The laser pulses employed as the optical pump were generated by doubling the output of a Ti:sapphire laser, yielding 400 nm laser pulses with an ∼15 ps FWHM at a 3 kHz repetition rate. The electron bunches stored in the APS ring delivered pulses with an 80 ps FWHM at 6.5 MHz repetition rate that were employed as an X-ray probe. The molecular complex $[Fe^{II}(tpen)](PF_6)_2$ was dissolved in acetonitrile (CH_3CN) to a concentration of 1.8 mM, which is below the solubility limit to avoid any clogging. The solution was continuously degassed by bubbling inert nitrogen. This liquid sample was then circulated inside an air-tight aluminum chamber through a stainless steel tube forming a free jet of 550 μm diameter so that the sample in the probed illuminated volume was fully replenished between two laser shots. In the region of spatial overlap, the X-ray spot size was 50 μm (V) x 450 μm (H) and the laser spot was 850 μm in diameter. The time delay between the optical and X-ray pulses (noted t) was controlled by a programmable delay line (PDL-100A-20NS, Colby Instruments): the phase shift of the mode-lock driver for the seed laser was varied relatively to that of the RF signal derived from the storage ring with a 500 fs precision. The incident X-ray energy was scanned over the Fe K edge (7709 eV) up to 700 eV above the 1s ionization threshold. Downstream, a metallic Fe foil was placed between two conventional ionization chambers. It was utilized for calibrating the X-ray energy, for correcting possible slow drifts, and for monitoring the X-ray flux in transmission mode. As detectors, two avalanche photodiodes (APDs) were placed on both sides at 90° angle from the pump−probe interaction region to collect the secondary emitted X-ray fluorescence photons. A combination of Soller slits with a $(Z - 1)$ Mn filter was inserted between the sample jet and the APD detectors, thereby reducing strongly the background due to elastic X-ray scattering. A third APD was employed to monitor the intensity of the incident X-ray beam. For signal processing, the outputs of the two APDs were fed to two fast analyzer cards (Agilent) that were triggered at 3 kHz by some scattered laser light purposely directed onto an additional photodiode. The X-ray fluorescence signals were then digitized by the card as a function of time at 1 ns/point following each trigger pulse. The fluorescence signals from the synchronized X-ray pulse at a delay t of 150 ps after the laser pulse pump excitation were accumulated to construct the TXAS trace $\mu_{laser\_on}(t)$. The fluorescence signals from the same X-ray pulse averaged over the 50 round trips in the storage ring that precede the pump event were recorded to construct the corresponding TXAS trace μ_{laser_off} for the complex in the ground state. The acquisition software performed the shot-to-shot normalization of the X-ray pulse intensities. Following such a data acquisition scheme, the $\mu_{laser\_on}(t)$ and μ_{laser_off} spectra were taken under the exact same experimental conditions for the sample, the laser, and the beamline status, which allowed canceling out any error associated to drifts. Building the difference signal $\Delta\mu = [\mu_{laser\_on}(t) - \mu_{laser\_off}]$ that stems from the fraction f of molecules in the excited state delivers the transient XA spectrum of the photoinduced HS state for $[Fe^{II}(tpen)]^{2+}$. The integrity of the sample was checked over time by comparing from scan to scan the lineshapes of the TXAS trace μ_{laser_off} in the XANES region. No change induced by possible radiation damage could be identified through the duration of the measurements.

TXAS Analysis and Fitting Procedure. The Horae suite was used for processing and analysis.[39−45] The Athena program was first employed to preprocess the experimental TXAS signal and to extract the normalized EXAFS function, $\chi(k)$, as a function of the photoelectron wave number, k, defined by

$$k = \sqrt{2m(E - E_0)}\,/\hbar$$

where m is the mass of photoelectron, E_0 is the absorption edge energy, and E is the incident X-ray energy.

Since the ground-state (GS) spectrum, μ_{laser_off}, and the excited (ES) spectrum, μ_{laser_on}, were measured simultaneously, the same normalization and background removal procedures were followed when extracting the experimental EXAFS function $\chi^{exp}_{GS}(k)$.

The Artemis program based on FEFF6 in Horae was then employed to fit $\chi^{exp}(k)$ to the theoretical expression of the oscillation amplitude in the EXAFS region $\chi^{theo}(k)$. This function was calculated according to

$$\chi^{theo}_{GS}(k) = \sum_i \frac{N_i S_0^2}{kR_i^2} F_i(k)\, e^{-2R_i/\lambda_i(k)}\, e^{-2k^2\sigma i}\, \sin[2kR_i]$$

DOI: 10.1021/acsomega.8b03688
ACS Omega 2019, 4, 6375−6381

where i indicates the ith shell of identical backscatters, N_i is the coordination number of the ith shell, S_0^2 is the amplitude reduction factor accounting for relaxation of the absorbing atom, $F_i(k)$ is the backscattering amplitude, R_i is the average distance between the center atom and backscatters, σ_i is the mean square variation in R_i, δ_i is the scattering phase shift due to the ith shell, and $\lambda_i(k)$ is the effective mean free path.

The geometry of the LS state obtained from the DFT optimization was taken as a starting guess for the GS structure of $[Fe^{II}(tpen)]^{2+}$ in CH_3CN. The contributions from all the paths in the first three scattering shells Fe−$N_{\alpha,\beta}$, Fe−$C_{\alpha,\beta,\gamma}$, and Fe−N−$C_{\alpha,\beta,\gamma,\delta}$ were included in the fitting. The atoms involved in those paths are labeled in Figure 3 of the main text. The shells share a common S_0^2 and σ_i^2. The parameters F_i, N_i, δ_i, and λ_i were calculated with FEFF6. The parameters R_i, σ_i^2, and E_0 were refined through the standard least-square minimization of the k^2-weighted EXAFS function, $k^2{*}\chi(k)$, with k ranging from 2.3 to 11.0 Å^{-1}. The Fourier transform of $k^2{*}\chi(k)$, with k ranging from 2.0 to 10.0 Å^{-1}, was fitted in R space in the range of 1−3.2 Å. The error bars were returned by Artemis.

For the ES, a set of excited EXAFS functions were constructed based on equation:

$$\chi_{ES}^{theo}(k) = \sum_i \frac{N_i S_0^2}{kR_i^2} F_i(k)\, e^{-2R_i/\lambda_i(k)}\, e^{-2k^2\sigma i} \sin[2kR_i]$$

where E_0, S_0^2, N_i, and σ_i^2 are fixed to the values obtained for the GS.

To reduce the number of free parameters, the variations in R were constrained by introducing the parameter ρ, defined as $R_{Fe-N\beta} = \rho.R_{Fe-N\alpha}$. The variable ρ was varied from 0.5 to 1.

Since the experimental EXAFS function for the ES state is extracted as

$$\chi_{ES}^{exp}(k) = \chi_{laser\_off}(k) + 1/f{*}[\chi_{laser\_on}(k) - \chi_{laser\_off}(k)]$$

the excited state fraction f needs to be considered as an extra fitting parameter. The geometry of the HS state obtained from the DFT optimization was taken as a starting guess for the ES structure. The fitting parameters and their error bars were extracted from a least-square minimization procedure, and the error bars were obtained from error propagation.[23]

■ ASSOCIATED CONTENT

Supporting Information

The Supporting Information is available free of charge on the ACS Publications website at DOI: 10.1021/acsomega.8b03688.

k^2-Weighted EXAFS function $\chi(k)$ for the μ_{laser_off} of $[Fe^{II}(tpen)]^{2+}$ solvated in acetonitrile and for a power sample of $[Fe^{II}(tpen)](PF_6)_2$ (PDF)

■ AUTHOR INFORMATION

Corresponding Author

*E-mail: sophie.canton@eli-alps.hu, sophie.canton@desy.de.

ORCID

Xiaoyi Zhang: 0000-0001-9732-1449

Karina Suarez-Alcantara: 0000-0002-8630-2899

Latévi Max Lawson Daku: 0000-0003-1305-6807

Sophie E. Canton: 0000-0003-4337-8129

Notes

The authors declare no competing financial interest.

■ ACKNOWLEDGMENTS

Dr. J. Zhang acknowledges funding from the National Natural Science Foundation of China (grant no. 21302138). The ELI-ALPS project (GINOP-2.3.6-15-2015-00001) is supported by the European Union and cofinanced by the European Regional Development Fund. Dr. S. E. Canton gratefully acknowledges funding from the Helmholtz Recognition Award. This research used resources of the Advanced Photon Source, US Department of Energy (DOE) Office of Science User Facilities operated for the DOE Office of Science by Argonne National Laboratory under Contract no. DE-AC02-06CH11357.

■ REFERENCES

(1) Hayami, S.; Holmes, S. M.; Halcrow, M. A. Spin-state switches in molecular materials chemistry. *J. Mater. Chem. C* **2015**, *3*, 7775−7778.

(2) Kumar, K. S.; Ruben, M. Emerging trends in spin crossover (SCO) based functional materials and devices. *Coord. Chem. Rev.* **2017**, *346*, 176−205.

(3) Halcrow, M. A. Halcrow, The foundation of modern spin-crossover. *Chem. Commun.* **2013**, *49*, 10890−10892.

(4) Luan, J.; Zhou, J.; Liu, Z.; Zhu, B. W.; Wang, H. S.; Bao, X.; Liu, W.; Tong, M.-L.; Peng, G.; Peng, H. N.; Salmon, L.; Bousseksou, A. Polymorphism-Dependent Spin-Crossover: Hysteretic Two-Step Spin Transition with an Ordered [HS−HS−LS] Intermediate Phase. *Inorg. Chem.* **2015**, *54*, 5145−5147.

(5) Létard, J.-F.; Asthana, S.; Shepherd, H. J.; Guionneau, P.; Goeta, A. E.; Suemura, N.; Ishikawa, R.; Kaizaki, S. Photomagnetism of a sym-cis-Dithiocyanato Iron(II) Complex with a Tetradentate N,N′-Bis(2-pyridylmethyl)1,2-ethanediamine Ligand. *Chem. - Eur. J.* **2012**, *18*, 5924−5934.

(6) Matouzenko, G. S.; Bousseksou, A.; Lecocq, S.; Van Koningsbruggen, P. J.; Perrin, M.; Kahn, O.; Collet, A. Spin Transition in [Fe(DPEA)(NCS)2], a Compound with the New Tetradentate Ligand (2-Aminoethyl)bis(2-pyridylmethyl)amine (DPEA):- Crystal Structure, Magnetic Properties, and Mössbauer Spectroscopy. *Inorg. Chem.* **1997**, *36*, 2975−2981.

(7) Matouzenko, G. S.; Bousseksou, A.; Lecocq, S.; Van Koningsbruggen, P. J.; Perrin, M.; Kahn, O.; Collet, A. Polymorphism in Spin Transition Systems. Crystal Structure, Magnetic Properties, and Mössbauer Spectroscopy of Three Polymorphic Modifications of [Fe(DPPA)(NCS)2] [DPPA = (3-Aminopropyl)bis(2-pyridylmethyl)amine]. *Inorg. Chem.* **1997**, *36*, 5869−5879.

(8) Stock, P.; Deck, E.; Hohnstein, S.; Korzekwa, J.; Meyer, K.; Heinemann, F. W.; Breher, F.; Hörner, G. Molecular Spin Crossover in Slow Motion: Light-Induced Spin-State Transitions in Trigonal Prismatic Iron(II) Complexes. *Inorg. Chem.* **2016**, *55*, 5254−5265.

(9) Al-Obaidi, A. H. R.; Jensen, K. B.; McGarvey, J. J.; Toftlund, H.; Jensen, B.; Bell, S. E. J.; Carroll, J. G. Structural and Kinetic Studies of Spin Crossover in an Iron(II) Complex with a Novel Tripodal Ligand. *Inorg. Chem.* **1996**, *35*, 5055−5060.

(10) Beheshti, A.; Lalegani, A.; Bruno, G.; Rudbari, H. A. Investigating the effect of flexible ligands on the crystal engineering of the iron(II) coordination compounds. *J. Mol. Struct.* **2013**, *1051*, 244−249.

(11) Toftlund, H.; McGarvey, J. J. Iron (II) spin crossover systems with multidentate ligands. *Top. Curr. Chem.* **2004**, *232*, 151−166.

(12) Hathcock, D. J.; Stone, K.; Madden, J.; Spencer, J. Slattery, Electron donating substituent effects on redox and spin state properties of iron(II) bis-terpyridyl complexes. *Inorg. Chim. Acta* **1998**, *282*, 131−135.

(13) Toftlund, H. Spin equilibria in iron(II) complexes. *Coord. Chem. Rev.* **1984**, *94*, 67−108.

(14) Chergui, M. Time-resolved X-ray spectroscopies of chemical systems: New perspectives. *Struct. Dyn.* **2016**, *3*, No. 031001.

(15) Chen, L. X. X-ray Transient Absorption Spectroscopy. *X-Ray Absorption and X-Ray Emission Spectroscopy: Theory and Applications*;

DOI: 10.1021/acsomega.8b03688
ACS Omega 2019, 4, 6375−6381

van Bokhoven, J. A., Lamberti, C., Eds.; Wiley, 2015; Vol. *I*, pp 213−250.
(16) Kim, J.; Kim, K. H.; Oang, K. Y.; Lee, J. H.; Hong, K.; Cho, H.; Huse, N.; Schoenlein, R. W.; Kim, T. K.; Ihee, H. Tracking reaction dynamics in solution by pump−probe X-ray absorption spectroscopy and X-ray liquidography (solution scattering). *Chem. Commun.* **2016**, *52*, 3734−3749.
(17) Chergui, M.; et al. Photoinduced Structural Dynamics of Molecular Systems Mapped by Time-Resolved X-ray Methods. *Chem. Rev.* **2017**, *117*, 11025−11065.
(18) Gawelda, W.; Pham, V.-T.; Benfatto, M.; Zaushitsyn, Y.; Kaiser, M.; Grolimund, D.; Johnson, S. L.; Abela, R.; Hauser, A.; Bressler, C.; Chergui, M. Structural determination of a short-lived excited iron (II) complex by picosecond x-ray absorption spectroscopy. *Phys. Rev. Lett.* **2007**, *98*, No. 057401.
(19) Gawelda, W.; Pham, V.-T.; van der Veen, R. M.; Grolimund, D.; Abela, R.; Chergui, M.; Bressler, C. Structural analysis of ultrafast extended x-ray absorption fine structure with subpicometer spatial resolution: Application to spin crossover complexes. *J. Chem. Phys.* **2009**, *130*, No. 124520.
(20) Nozawa, S.; Sato, T.; Chollet, M.; Ichiyanagi, K.; Tomita, A.; Fujii, H.; Adachi, S.; Koshihara, S. Direct Probing of Spin State Dynamics Coupled with Electronic and Structural Modifications by Picosecond Time-Resolved XAFS. *J. Am. Chem. Soc.* **2010**, *132*, 61−63.
(21) Khalil, M.; Marcus, M. A.; Smeigh, A. L.; McCusker, J. K.; Chong, H. H. W.; Schoenlein, R. W. Picosecond X-ray Absorption Spectroscopy of a Photoinduced Iron(II) Spin Crossover Reaction in Solution. *J. Phys. Chem. A* **2006**, *110*, 38−44.
(22) Zhan, F.; Tao, Y.; Zhao, H. Alternative difference analysis scheme combining R-space EXAFS fit with global optimization XANES fit for X-ray transient absorption spectroscopy. *J. Synchrotron Rad.* **2017**, *24*, 818−824.
(23) Liu, C.; Zhang, J.; Lawson Daku, L. M.; Gosztola, D.; Canton, S. E.; Zhang, X. Probing the Impact of Solvation on Photoexcited Spin Crossover Complexes with High-Precision X-ray Transient Absorption Spectroscopy. *J. Am. Chem. Soc.* **2017**, *139*, 17518−17524.
(24) Cammarata, M.; Bertoni, R.; Lorenc, M.; Cailleau, H.; Di Matteo, S.; Mauriac, C.; Matar, S. F.; Lemke, H.; Chollet, M.; Ravy, S.; Laulhé, C.; Létard, J.-F.; Collet, E. Sequential Activation of Molecular Breathing and Bending during Spin-Crossover Photoswitching Revealed by Femtosecond Optical and X-Ray Absorption Spectroscopy. *Phys. Rev. Lett.* **2014**, *113*, No. 227402.
(25) Zerdane, S.; Collet, E.; Dong, X.; Matar, S. F.; Wang, H. F.; Desplanches, C.; Chastanet, G.; Chollet, M.; Glownia, J. M.; Lemke, H. T.; Lorenc, M.; Cammarata, M. Electronic and Structural Dynamics During the Switching of the Photomagnetic Complex [Fe(L222N5)(CN)2]. *Chem. Eur. J.* **2018**, *24*, 5064−5069.
(26) Canton, S. E.; Zhang, X. Y.; Daku, L. M. L.; Smeigh, A. L.; Zhang, J. X.; Liu, Y. Z.; Wallentin, C.-J.; Attenkofer, K.; Jennings, G.; Kurtz, C. A.; Gosztola, D.; Wärnmark, K.; Hauser, A.; Sundström, V. Probing the Anisotropic Distortion of Photoexcited Spin Crossover Complexes with Picosecond X-ray Absorption Spectroscopy. *J. Phys. Chem. C* **2014**, *118*, 4536−4545.
(27) Zhang, X. Y.; Lawson Daku, M. L.; Zhang, J. X.; Suarez-Alcantara, K.; Jennings, G.; Kurtz, C. A.; Canton, S. E. Dynamic Jahn−Teller Effect in the Metastable High-Spin State of Solvated [Fe(terpy)2]2+. *J. Phys. Chem. C* **2015**, *119*, 3312−3321.
(28) Vankó, G.; Bordage, A.; Pápai, M.; Haldrup, K.; Glatzel, P.; March, A. M.; Doumy, G.; Britz, A.; Galler, A.; Assefa, T.; et al. Detailed Characterization of a Nanosecond-Lived Excited State: X-ray and Theoretical Investigation of the Quintet State in Photoexcited [Fe(terpy)2]2+. *J. Phys. Chem. C* **2015**, *119*, 5888−5902.
(29) Chang, H. R.; McCusker, J. K.; Toftlund, H.; Wilson, S. R.; Trautwein, A. X.; Winkler, H.; Hendrickson, D. N. [Tetrakis(2-pyridylmethyl)ethylenediamine]iron(II) perchlorate, the first rapidly interconverting ferrous spin-crossover complex. *J. Am. Chem. Soc.* **1990**, *112*, 6814−6827.
(30) Blindauer, C. A.; et al. Metal complexes of N,N,N′,N′-tetrakis(2-pyridylmethyl)ethylenediamine (TPEN): Variable coordination numbers and geometries. *Polyhedron* **2006**, *25*, 513−520.
(31) Chen, G.; Espinosa-Perez, G.; Zentella-Dehesa, A.; Silaghi-Dumitrescu, I.; Lara-Ochoa, F. (Tetrakis(2-pyridylmethyl)-ethylenediamine)iron(II) Perchlorate. Study of Density Functional Methods. *Inorg. Chem.* **2000**, *39*, 3440.
(32) Solans, X.; Ruiz-Ramirez, L.; Moreno-Esparza, R.; Labrador, M.; Escuer, A. (Tetrakis(2-pyridylmethyl)ethylenediamine)iron(II) Perchlorate. Phase Transition Study about the First Rapidly Interconverting Ferrous Spin-Crossover Complex. *J. Solid State Chem.* **1994**, *109*, 315−320.
(33) McGarvey, J. J.; Toftlund, H.; Al-Obaidi, A. H. R.; Taylor, K. P.; Bell, S. E. J. Photoperturbation of the 1A .dblharw. 5T spin equilibrium in an iron(II) complex in solution via ligand field excitation. *Inorg. Chem.* **1993**, *32*, 2469−2472.
(34) McCusker, J. K.; Walda, K. N.; Dunn, R. C.; Simon, J. D.; Magde, D.; Hendrickson, D. N. Sub-picosecond .DELTA.S = 2 intersystem crossing in low-spin ferrous complexes. *J. Am. Chem. Soc.* **1992**, *114*, 6919−6920.
(35) McCusker, J. K.; Walda, K. N.; Dunn, R. C.; Simon, J. D.; Magde, D.; Hendrickson, D. N. Subpicosecond 1MLCT.→ 5T2 intersystem crossing of low-spin polypyridyl ferrous complexes. *J. Am. Chem. Soc.* **1993**, *115*, 298−307.
(36) McCusker, J. K.; Toftlund, H.; Rheingold, A. L.; David, N. Hendrickson Ligand conformational changes affecting 5T2. →. 1A1 intersystem crossing in a ferrous complex. *J. Am. Chem. Soc.* **1993**, *115*, 1797−1804.
(37) McCusker, J. K.; Rheingold, A. L.; Hendrickson, D. N. Variable-Temperature Studies of Laser-Initiated 5T2 → 1A1 Intersystem Crossing in Spin-Crossover Complexes:? Empirical Correlations between Activation Parameters and Ligand Structure in a Series of Polypyridyl Ferrous Complexes. *Inorg. Chem.* **1996**, *35*, 2100−2112.
(38) Butcher, R. J. Structural aspects of the bis(2,2′-dipicolylamine)-iron(II) cation. *Inorg. Chim. Acta* **1989**, 211−215.
(39) Ravel, B.; et al. ATHENA, ARTEMIS, HEPHAESTUS: data analysis for X-ray absorption spectroscopy using IFEFFIT. *J. Synchrotron Radiat.* **2005**, *12*, 537.
(40) Newville, M. IFEFFIT: interactive EXAFS analysis and FEFF fitting. *J. Synchrotron Radiat.* **2001**, *8*, 322.
(41) Frisch, M. J.; Trucks, G. W.; Schlegel, H. B.; Scuseria, G. E.; Robb, M. A.; Cheeseman, J. R.; Scalmani, G.; Barone, V.; Mennucci, B.; Petersson, G. A.; Nakatsuji, H.; Caricato, M.; Li, X.; Hratchian, H. P.; Izmaylov, A. F.; Bloino, J.; Zheng, G.; Sonnenberg, J. L.; Hada, M.; Ehara, M.; Toyota, K.; Fukuda, R.; Hasegawa, J.; Ishida, M.; Nakajima, T.; Honda, Y.; Kitao, O.; Nakai, H.; Vreven, T.; Montgomery, J. A., Jr.; Peralta, J. E.; Ogliaro, F.; Bearpark, M.; Heyd, J. J.; Brothers, E.; Kudin, K. N.; Staroverov, V. N.; Keith, T.; Kobayashi, R.; Normand, J.; Raghavachari, K.; Rendell, A.; Burant, J. C.; Iyengar, S. S.; Tomasi, J.; Cossi, M.; Rega, N.; Millam, J. M.; Klene, M.; Knox, J. E.; Cross, J. B.; Bakken, V.; Adamo, C.; Jaramillo, J.; Gomperts, R.; Stratmann, R. E.; Yazyev, O.; Austin, A. J.; Cammi, R.; Pomelli, C.; Ochterski, J. W.; Martin, R. L.; Morokuma, K.; Zakrzewski, V. G.; Voth, G. A.; Salvador, P.; Dannenberg, J. J.; Dapprich, S.; Daniels, A. D.; Farkas, O.; Foresman, J. B.; Ortiz, J. V.; Cioslowski, J.; Fox, D. J. *Gaussian 09*, revision D.01; Gaussian, Inc.: Wallingford CT, 2013.
(42) Perdew, J. P.; et al. Generalized Gradient Approximation Made Simple John P. Perdew, Kieron Burke, and Matthias Ernzerhof. *Phys. Rev. Lett.* **1996**, *77*, 3865.
(43) Grimme, S.; Antony, J.; Ehrlich, S.; Krieg, H. A consistent and accurate ab initio parametrization of density functional dispersion correction (DFT-D) for the 94 elements H-Pu. *J. Chem. Phys.* **2010**, *132*, No. 154104.
(44) Schäfer, A.; Huber, C.; Ahlrichs, R. Fully optimized contracted Gaussian basis sets of triple zeta valence quality for atoms Li to Kr. *J. Chem. Phys.* **1994**, *100*, 5829.

DOI: 10.1021/acsomega.8b03688
ACS Omega 2019, 4, 6375−6381

(45) Tomasi, J.; et al. Quantum Mechanical Continuum Solvation Models Jacopo Tomasi, Benedetta Mennucci, and Roberto Cammi. *Chem. Rev.* **2005**, *105*, 2999−3094.

DOI: 10.1021/acsomega.8b03688
ACS Omega 2019, 4, 6375−6381